Journal of Materials Chemistry A

ROYAL SOCIETY OF CHEMISTRY

PAPER

View Article Online
View Journal | View Issue

Cite this: *J. Mater. Chem. A*, 2020, **8**, 15951

Catalytic activity atlas of ternary Co–Fe–V metal oxides for the oxygen evolution reaction†

Junsheng Chen,[a] Hao Li,[b] Zengxia Pei,[a] Qianwei Huang,[c] Ziwen Yuan,[a] Chaojun Wang,[a] Xiaozhou Liao,[c] Graeme Henkelman,[b] Yuan Chen *[a] and Li Wei *[a]

Received 15th April 2020
Accepted 1st June 2020

DOI: 10.1039/d0ta04088f

rsc.li/materials-a

The sluggish oxygen evolution reaction (OER) is a crucial limiting factor in many renewable energy conversion and storage devices. Multi-metal oxides have been explored as efficient electrocatalysts for the OER; however, the ideal elemental composition for multi-metal oxides is unknown. We first performed density functional theory calculations, which predicted that Co oxyhydroxides doped with Fe and V have excellent catalytic activity. We synthesized a series of amorphous Co–Fe–V ternary metal oxides with a precisely controlled metal molar composition (denoted as $Co_aFe_bV_cO_x$, where $a + b + c = 10$), uniformly distributed elements and identical morphologies by using Prussian blue analogues (PBAs) as novel metal precursors. A systematic investigation was carried out to establish correlations between the elemental compositions and the OER activity for $Co_aFe_bV_cO_x$, resulting in a comprehensive catalytic activity atlas of ternary Co–Fe–V metal oxides for the OER, which can serve as a roadmap for electrocatalyst development. In particular, $Co_3Fe_4V_3O_x$ with an elemental composition of Co : Fe : V = 3 : 4 : 3 shows the best performance, with an overpotential of merely 249 mV to reach a current density of 10 mA cm^{-2}, and a low Tafel slope of 41 mV dec^{-1}, outperforming a commercial IrO_x catalyst. X-ray photoelectron spectroscopy analysis reveals strong electronic synergies among the metal cations in $Co_aFe_bV_cO_x$. The V and Fe doping can affect the electronic structure of Co to yield nearly optimal adsorption energies for OER intermediates, giving rise to the superior activity. Furthermore, composition-tuneable and uniform PBAs may serve as versatile and efficient metal precursors to produce many more multi-metal oxides for various renewable energy applications.

Introduction

The oxygen evolution reaction (OER) is a vital reaction in many different types of sustainable energy storage and conversion devices, such as metal–air batteries and water electrolyzers.[1,2] Multiple electron-proton coupled transfer steps of the OER lead to sluggish kinetics and require a high overpotential, which limits device performance and increases operating costs.[3] Noble metal oxides, such as IrO_2 and RuO_2, show the highest catalytic activities for the OER. However, their scarcity, high-cost, and poor stability are significant obstacles for practical applications.[4] Therefore, developing efficient, low-cost, and durable catalysts for the OER is a critical task. Transition metal based-materials, such Co, Fe, and Ni, are being extensively studied as alternative electrocatalysts for the OER because of their abundance, low-cost and relatively high catalytic activities.[5,6] Previous studies reported that bi- or tri-metallic oxides and hydroxides of Co, Fe, and Ni, such as Co–Fe, Ni–Fe, and Co–Fe–Ni oxides, have higher catalytic activity than their mono-metallic counterparts.[7–16] In 2016, Zhang *et al.* reported that Co–Fe oxyhydroxides incorporated with W (Co–Fe–W) have a very high catalytic activity for the OER.[17] They proposed that the empty d-electron orbitals of high-valence W^{6+} can effectively interact with Co atoms in the Co–Fe–W oxyhydroxides, resulting in a near-optimal electronic structure for the adsorption of OER intermediates. In this direction, other high-valence ions, such as Mo^{6+} and Cr^{3+}, have also been explored to enhance the OER catalytic activity of transition metal oxides and hydroxides.[18,19] Because redox-active V has +3, +4, and +5 states and is capable of actively interacting with Co, two studies have reported trimetallic Co–Fe–V oxides and spinels as OER electrocatalysts.[20,21] However, the exact roles of V in these Co–Fe–V oxide-based OER electrocatalysts are still poorly understood. A critical obstacle is the difficulty in incorporating V into Co–Fe oxides to obtain Co–Fe–V oxides with well-defined structures.

[a]School of Chemical and Biomolecular Engineering, The University of Sydney, Sydney, New South Wales, 2006, Australia. E-mail: yuan.chen@sydney.edu.au; l.wei@sydney.edu.au

[b]Department of Chemistry, The Oden Institute for Computational Engineering and Sciences, The University of Texas at Austin, 105 E. 24th Street, Stop A5300, Austin, Texas, 78712, USA

[c]School of Aerospace, Mechanical and Mechatronic Engineering, The University of Sydney, Sydney, New South Wales, 2006, Australia

† Electronic supplementary information (ESI) available. See DOI: 10.1039/d0ta04088f

Herein, we first carried out density functional theory (DFT) calculations to predict potential ideal structures of Co–Fe–V oxides to serve as OER electrocatalysts. Guided by our theoretical calculations, we synthesized Prussian blue analogue (PBA) nanoparticles with precise atomic structures. We used them as metal precursors to obtain amorphous Co, Fe, and V mono-, bi- or tri-metal oxides with tuneable, yet accurately controlled, compositions. Using these metal oxides, we established the first comprehensive elemental composition–OER catalytic activity atlas for amorphous Co–Fe–V oxides. The atlas indicates that Co–Fe–V oxides at the optimal Co : Fe : V molar ratio of 3 : 4 : 3 outperform RuO_2 and IrO_2 in both activity and stability for the OER. The electronic interactions among Co, Fe, and V in Co–Fe–V metal oxides were further studied by X-ray photoelectron spectroscopy (XPS).

Experimental section

Computational methods

DFT calculations were conducted using the Vienna *Ab initio* Simulation Package. Core electrons were described within the projector augmented-wave framework.[22] The generalized gradient approximation method was employed to describe electron correlation, with a revised Perdew–Burke–Ernzerhof functional.[23,24] Kohn–Sham wave functions expanded in a plane wave basis set were used to describe the valence electrons.[25] The Brillouin zone was sampled with $(3 \times 3 \times 1)$ Monkhorst–Pack *k*-point mesh, using the method developed by Methfessel and Paxton.[26] Spin-polarization and Hubbard-U corrections (DFT + U) were considered for all calculations. The convergence for all calculations was defined when the force on each atom was lower than 0.01 eV $Å^{-1}$. U_{eff} (U–J) values of 3.52, 4.00, and 3.40 eV were applied to Co, Fe, and V, respectively. Dipole moment corrections were considered in all calculations to correct residual dipole moments perpendicular to the slab model. Entropic corrections (for gas-phase molecules) and zero-point energies were also considered for the free energy calculations. The Co oxyhydroxide (CoOOH) surface was selected as the base model due to its high reactivity and stability for the OER,[27] as modelled with a 4-layer (2×3) $(10\bar{1}4)$ slab. Other bi- and tri-metallic CoOOH surfaces were developed by replacing surface Co atoms with Fe and/or V atoms.

Materials synthesis

All chemicals were purchased from Sigma-Aldrich. PBA nanoparticles were synthesized by a co-precipitation method. Briefly, Co^{2+}, Fe^{2+} and VO^{2+} precursor solutions were prepared at a concentration of 50 mM by dissolving $CoCl_2$, $FeCl_2$, and $VOSO_4$, in deionized water. A metal cation solution was prepared by mixing an appropriate amount of precursor solutions and diluted with DI H_2O to 50 mL to achieve a total cation concentration of 30 mM (total 1.5 mmol, denoted as solution A, see details in Table S1 in the ESI†). $K_3Fe(CN)_6$ and $K_3Co(CN)_6$ solutions of 20 mM concentration were prepared and mixed accordingly to prepare the $M(CN)_6^{3-}$ solution at a concentration of 20 mM (1.0 mmol, denoted as solution B). Next, solution A was slowly added to solution B at a rate of 1 mL min^{-1} under vigorous stirring. The mixture was further stirred for 2 h to allow the formation of Co–Fe–V PBA nanoparticles. The resulting solid materials were recovered by centrifugation at 4500*g* followed by washing with deionized water and ethanol three times each. Fe PB, Fe–Co PBA, and Fe–V PBA nanoparticles were synthesized using the same method while changing the corresponding metal cation solution with the same total metal concentration of 1.5 mmol. The synthesis method used for Co and Co–V PBA nanoparticles was similar except that potassium hexacyanocobaltate ($K_3[Co(CN)_6]$) was used. The washed solid materials were dried at 80 °C for 24 h in a vacuum oven. Next, they were oxidatively decomposed under an airflow of 20 sccm for 1 h at 300 °C to yield Co–Fe–V metal oxides. A series of samples with different metal ratios were synthesized. They are denoted as $Co_aFe_bV_{1-a-b}O_x$, where *a* and *b* represent the molar fraction of Co and Fe, respectively.

Materials characterization

The crystal structures of $Co_aFe_bV_{1-a-b}O_x$ were examined by X-ray diffraction (XRD, PANalytical X'Pert Powder) in the 2θ range of 5–80°. Their thermal gravimetric analysis (TGA) profiles were collected on a TGA instrument (Perkin Elmer, Pyris Diamond). Raman spectra were collected on a Renishaw inVia microscope with an excitation laser of 532 nm at a power density of 0.1 mW cm^{-2}. The morphology and elemental distribution of the PBA nanoparticles and metal oxides were characterized using a scanning electron microscope (SEM, JEOL, JSM-6700F) and transmission electron microscope (TEM, FEI, ThemisZ) with energy-dispersive X-ray spectroscopy (EDX) elemental mapping performed at an accelerating voltage of 200 kV. XPS spectra were collected on a Thermo Scientific K-Alpha instrument with an Al Kα source at a pass energy of 20 eV with the flood gun turned on. A standard graphite reference sample was used for energy calibration.

Electrochemical characterization

A chemical workstation (CHI 760E) was used to investigate the catalytic performance of $Co_aFe_bV_{1-a-b}O_x$ for the OER in a three-electrode configuration. A glassy carbon electrode (GCE, 0.2 cm^2, Pine Instrument) was used as the working electrode, Pt gauze as the counter electrode, and a Hg/HgO (20% KOH) electrode as the reference electrode. A similar loading mass on the GCE was used for all samples to compare their performance better. All potentials were calibrated to a reversible hydrogen electrode using the equation $E_{RHE} = E_{Hg/HgO} + 0.059 \times pH + 0.098$. The GCE was polished using an alumina suspension before measurement of each sample. The electrocatalyst inks were prepared by dispersing around 5 mg of each type of sample in a 1 mL mixed solution of water and isopropyl alcohol solution (1 : 9, v/v) containing 0.05 wt% Nafion 117 (Sigma-Aldrich), followed by bath sonication for 60 min to achieve a homogeneous suspension. Next, 8 μL of the as-prepared ink was drop-cast on the GCE to obtain an areal mass loading of 0.2 mg cm^{-2}. The electrodes were dried at room temperature overnight before testing. Commercial IrO_2 and RuO_2 (99.9%, Sigma-

Aldrich) were used as the reference. Electrochemical testing was performed in a three-cell electrolyser and the reference electrode was separated from the working electrode with a glass frit to avoid possible concentration crossover. Pure O_2 gas was purged for 30 min in a 1 M KOH electrolyte before performing measurements. The electrocatalyst was pre-conditioned by cycling it at a scan rate of 50 mV s^{-1} between 1 and 1.6 V *vs.* RHE for 50 cycles before commencing electrochemical performance testing. Linear sweep voltammetry (LSV) curves were obtained at a scan rate of 5 mV s^{-1} with 95% iR-compensation. The tests were performed on a rotating disk electrode at 1600 rpm to remove any generated bubbles. The electrochemically active surface area (ECSA) of different samples was measured by the cyclic voltammetry (CV) method. Briefly, the CV curves of an electrocatalyst loaded on a GCE were collected at scan rates of 2, 5, 10, 20 and 50 mV s^{-1} between 0.92 and 0.96 V *vs.* RHE in a 1 M KOH electrolyte. The cathodic and anodic current density differences at 0.94 V *vs.* RHE were plotted and fitted linearly as a function of the scan rates. Half of the slope was taken as the electric double layer capacitance (C_{dl}) of the electrocatalyst. A specific capacitance (C_s) of 0.04 mF cm^{-2} was used for calculating the ECSA using the following equation,[28] where A is the geometric area of the glassy carbon electrode (about 0.2 cm^2):

$$\text{ECSA} = \frac{AC_{dl}}{C_s}$$

Electrochemical impedance spectroscopy Nyquist plots of different samples were collected at an overpotential of 250 mV from 10^5 to 0.1 Hz with an amplitude of 5 mV. The faradaic efficiency was determined by a rotary ring-disk electrode method in an Ar saturated 1 M KOH electrolyte according to a reported method.[17] The catalyst was loaded on the glassy carbon disk and biased at 1.45 V *vs.* RHE while the Pt ring was maintained at 0.4 V *vs.* RHE to reduce the oxygen produced from the catalyst. The efficiency is calculated using:

$$\text{faradaic efficiency (\%)} = \frac{|I_{ring}|}{NI_{disk}} \times 100\%$$

where I_{ring} and I_{disk} are the current on the ring and disk electrode, respectively. N is the collection efficiency of the RRDE (E6R2, Pine Instrument). The calibrated N value is 0.376.

TOF and mass activity calculation

Turnover frequencies (TOFs) and mass activities at $\eta = 300$ mV (1.53 V *vs.* RHE) were calculated using:[29–31]

$$\text{TOF} = \frac{I}{4nF}$$

$$\text{Mass activity} = \frac{I}{m}$$

where I is the current at $\eta = 350$ mV, F is the Faraday constant (96 485 C mol^{-1}), n is the mole number of the metal in the catalyst and m is the total mass loaded on the electrode. The value of n is determined using the following equation:

$$n = \frac{m}{M_w}$$

where m is the mass of the total catalyst loaded on the electrode and M_w is the molar weight of the catalyst. The oxygen contents in different samples were determined from the XPS survey scan.

Results and discussion

Several recent studies have shown that metal oxide catalysts often become restructured to form oxyhydroxides, which serve as the real catalytically active sites for the OER.[32,33] Due to the complexity of modeling ternary or even higher metal oxide mixtures, we used Co oxyhydroxide (β-CoOOH) as a model catalyst for Co oxides to perform DFT calculations to examine the effects of incorporating Fe and V and estimate site-specific catalytic activities.[34] As illustrated in Fig. 1a, trimetallic Co–Fe–V, and bimetallic Co–Fe and Co–V oxyhydroxides were modelled by replacing Co atoms with Fe and/or V atoms in the monometallic β-CoOOH slab with exposed $(10\bar{1}4)$ facets.[35] The calculated total density of states (DOS) profiles of these models are compared in Fig. 1b (top panel). The trimetallic Co–Fe–V oxyhydroxide exhibits the highest electron density near the Fermi level (E_f, −0.5–0.5 eV), providing higher electrical conductivity, which is beneficial for the OER.[36] Further, Fig. 1b (bottom panel) shows that the trimetallic Co–Fe–V oxyhydroxide exhibits the highest Co 3d electron density near the Fermi level, indicating that the incorporation of Fe and V can strongly influence the electronic structure of Co. This DFT result supports the hypothesis that a near-optimal electronic structure for interacting with OER intermediates can be achieved by tuning the Fe and V doping in Co oxyhydroxide.[17]

We further performed detailed DFT calculations to determine OER free energy profiles on the different oxyhydroxide models according to the commonly used four-step OER mechanism below:[32]

$$H_2O + * \rightarrow OH^* + H^+ + e^- \quad (1)$$

$$OH^* \rightarrow O^* + H^+ + e^- \quad (2)$$

$$H_2O + O^* \rightarrow OOH^* + H^+ + e^- \quad (3)$$

$$OOH^* \rightarrow O_2 + H^+ + e^- + * \quad (4)$$

where * stands for a surface-active site. A computational hydrogen electrode method is adopted here; therefore, the theoretical overpotentials calculated from (1)–(4) are expected to be independent of pH or potential values, since the free energies shift in the same direction with varying pH and applied potential, resulting in the same potential determining step.[37] Previous studies also indicated that the theoretical overpotentials calculated using this mechanism led to good agreement with experimental OER overpotentials for oxides in both alkaline and acidic solutions.[37] The calculated free energy profiles are displayed in Fig. 1c. A highly efficient OER electrocatalyst is expected to have moderate adsorption energies for OH*, O* and OOH* intermediates.[38] Our DFT results show that

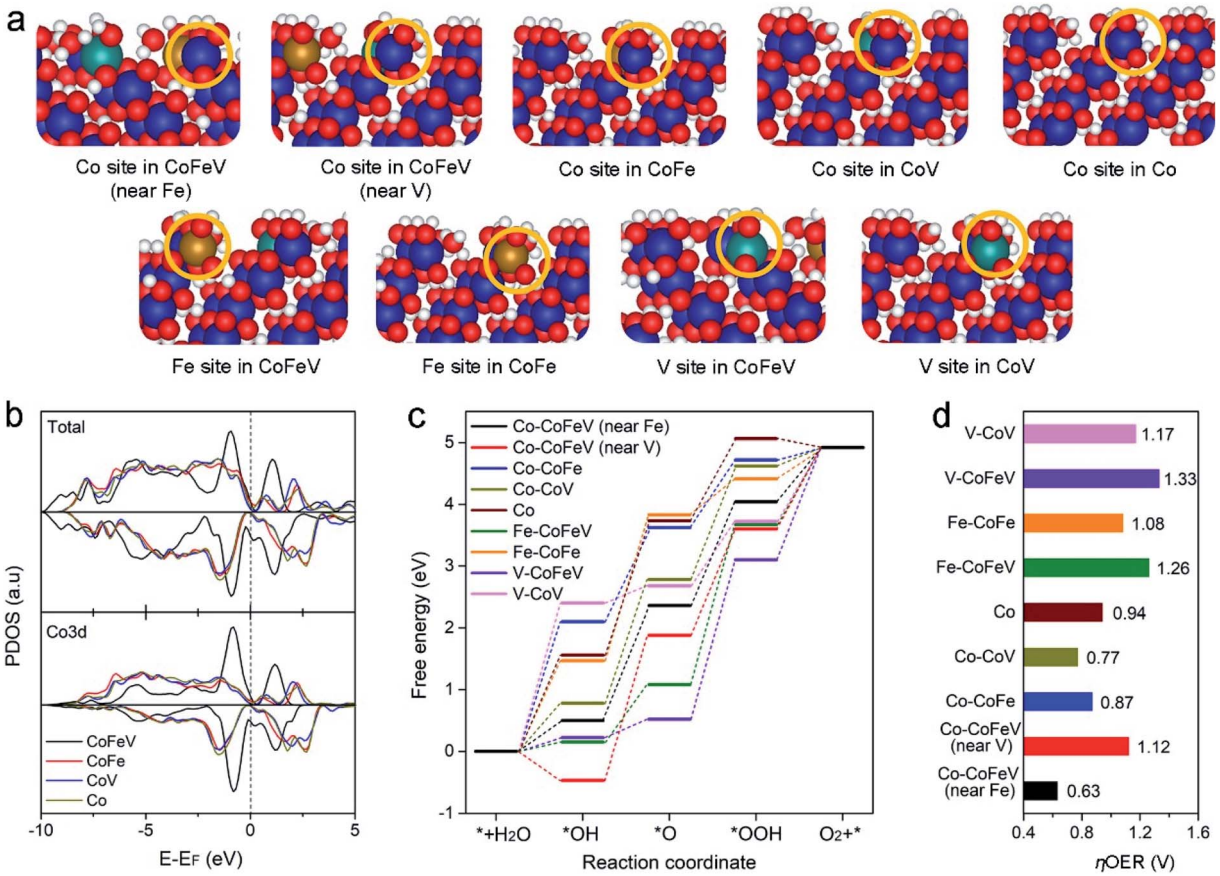

Fig. 1 (a) Schematic illustrations of nine different Co, Fe and V sites in trimetallic Co–Fe–V, bimetallic Co–Fe and Co–V and monometallic CoOOH models. Atoms: Co-blue, Fe-brown, V-green, O-red, and H-white. (b) Total DOS and the contribution from Co in the four models. (c) Calculated site-specific free energy diagrams of the five types of Co sites and other Fe and V sites shown in (a). (d) Theoretical onset overpotential (η_{OER}) of various sites.

the incorporation of Fe and V can change the adsorption energy of various OER intermediates substantially in comparison to the original CoOOH model. In particular, V doping can lower the energy for initial OH adsorption, which is beneficial for the OER. The theoretical overpotentials of different Co-sites were determined using $\eta_{OER} = G_{OER}/e - 1.23$ V, where $G_{OER} = \max[\Delta G_1, \Delta G_2, \Delta G_3, \Delta G_4]$. As displayed in Fig. 1d, the Co site near Fe in the Co–Fe–V trimetallic model displays the lowest η_{OER} compared to other Co sites as well as Fe and V sites in these models, indicating its superior catalytic activity. However, the possibility of Fe serving as OER active sites cannot be ruled out.[17,39] This encouraging qualitative estimation further confirms that Co–Fe–V trimetallic oxides with an optimized elemental composition may serve as an efficient OER electrocatalyst.

To synthesize such Co–Fe–V trimetallic oxides with tunable compositions (denoted as $Co_aFe_bV_cO_x$, where $a + b + c = 10$), we focussed on PBAs. PBAs are a family of metal-cyanide based coordinated materials with tunable elemental compositions and controllable morphology and they have been utilized as precursors to form OER electrocatalysts.[40–42] We envisioned that PBAs could be used as metal precursors to synthesize metal oxides with precisely controlled compositions. The synthesis scheme of various PBA derived Co–Fe–V metal oxides is illustrated in Fig. 2a. PBA nanoparticles with different compositions but identical morphology were first synthesized by a co-precipitation method by mixing Co^{2+}, VO^{2+}, Fe^{2+}, $Fe(CN)_6^{3-}$ and $Co(CN)_6^{3-}$ precursor solutions in different volumetric ratios (see the Experimental section for details). The slow crystallization and precipitation during the co-precipitation enable the precise control of elemental composition and metal distribution in the resulting PBA nanoparticles.[43] Solid PBA nanoparticles were recovered from their synthesis solutions by centrifugation and then repeatedly washed before drying. Afterward, these PBA nanoparticles were thermally decomposed at 300 °C in air to obtain the corresponding amorphous metal oxide nanoparticles.

The powder X-ray diffraction (XRD) patterns of one type of representative PBA nanoparticle (with a molar ratio of Co : Fe : V of 3 : 4 : 3, denoted as $Co_3Fe_4V_3$) and its corresponding thermally annealed metal oxide nanoparticles ($Co_3Fe_4V_3O_x$) are displayed in Fig. 2b. The XRD pattern of the PBA nanoparticles exhibits well-resolved diffraction peaks at 2θ values of 17.4, 24.7, 35.2, and 39.5 degrees, which can be assigned to the (100), (110), (200) and (210) facets of the Prussian blue (PB) lattice according to the standard PDF card (#01-

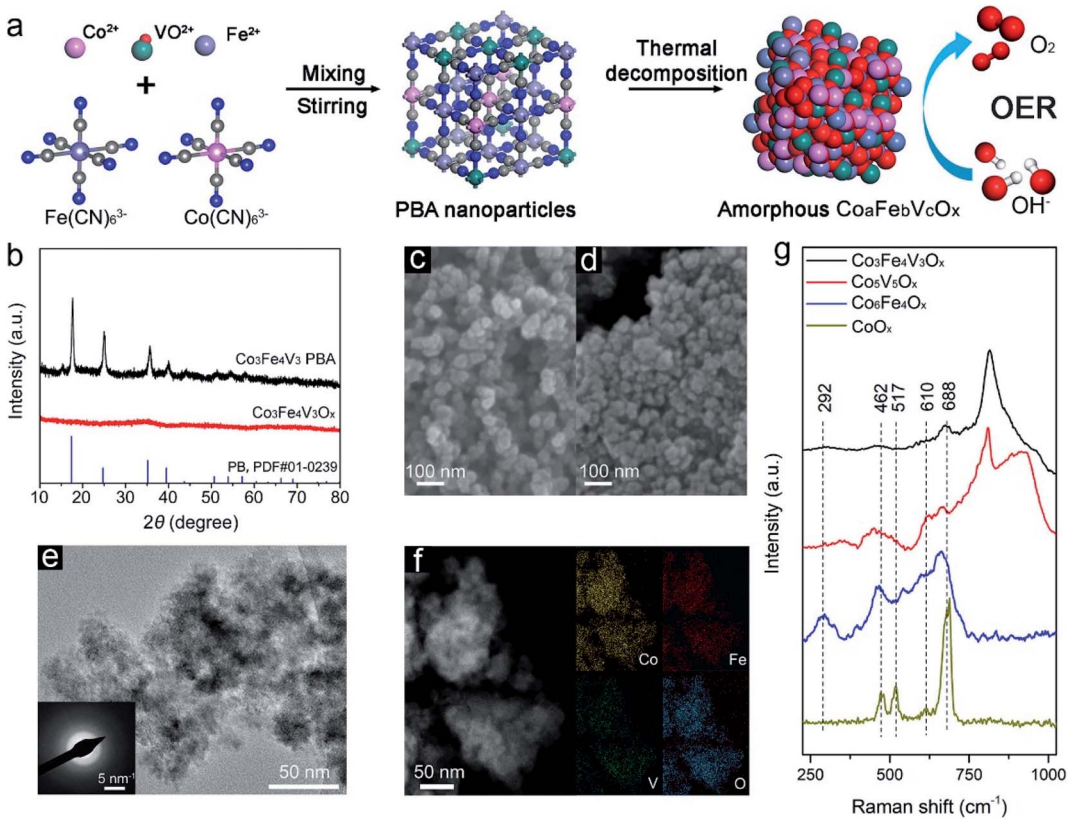

Fig. 2 (a) The schematic illustration of the synthesis method used to obtain various metal oxides from PBA nanoparticles. (b) XRD patterns and SEM images of (c) $Co_3Fe_4V_3$ PBA and (d) the resulting $Co_3Fe_4V_3O_x$ nanoparticles. (e) A TEM image (the corresponding SAED pattern in the inset) and (f) a HAADF-STEM image and the corresponding EDX elemental maps of $Co_3Fe_4V_3O_x$ nanoparticles. (g) Raman spectra of different oxides.

0239). Other PB/PBA nanoparticles used in this study all exhibit similar diffraction patterns (see Fig. S1 in the ESI†). There are minor peak shifts for PBA nanoparticles in comparison to the PB sample, which can be attributed to the atomic size differences between Co (or V) and Fe in the unit cells.[44] After thermal annealing in air, the PBA nanoparticles were thermally decomposed into metal oxides. The featureless XRD patterns displayed in Fig. 2b and S2 in the ESI† indicate that the PBA lattices were fully decomposed into amorphous metal oxides. We found that the thermal annealing temperature of PBA nanoparticles is critical for controlling the crystallinity of the resulting metal oxide nanoparticles. A TGA profile of the $Co_3Fe_4V_3$ PBA nanoparticles was recorded in air. Two major weight loss peaks were observed between 260 and 310 °C (see Fig. S3 in the ESI†). The corresponding thermal flow profile shows two peaks at 265 and 320 °C, which can be assigned to the thermal decomposition and crystallization of the amorphous metal oxides, respectively.[45] Therefore, we set the annealing temperature of the PBA nanoparticles to 300 °C to produce amorphous metal oxide nanoparticles. A crystalized reference sample was also prepared by thermal annealing of $Co_3Fe_4V_3$ PBA nanoparticles at 350 °C (denoted as $Co_3Fe_4V_3O_x$-C). Fig. S4 in the ESI† shows that various phase-segregated metal oxides can be observed from their XRD patterns.

The surface morphology of the PBAs and the resulting metal oxide nanoparticles was examined using a SEM. As shown in Fig. 2c, the $Co_3Fe_4V_3$ PBA nanoparticles exhibit a uniform particle geometry with an average diameter of about 54 nm, while the resulting $Co_3Fe_4V_3O_x$ nanoparticles show similar morphology (Fig. 2d). However, the average particle diameter slightly decreases from 54 nm to about 50 nm (Table S2 in the ESI†). The morphologies of other PBAs and their corresponding metal oxide nanoparticles are also comparable. All PBA and PB precursors exhibit similar particulate morphologies with comparable diameters (Fig. S5 and Table S2 in the ESI†). The only exception is the Co PBA nanoparticles, which exhibit a cubic structure with a greater particle size of ~97 nm (Fig. S5 in the ESI†). The particle size analysis results obtained using a TEM (Fig. 2e) are consistent with the SEM characterization results. No prominent lattice fringes are observed, and only diffuse rings are seen in the selected area electron diffraction (SAED) pattern in the inset of Fig. 2e. The high-angle annular dark-field scanning transmission electron microscope (HAADF-STEM) image and its corresponding EDX elemental mapping results are displayed in Fig. 2f. A uniform elemental distribution can be found in both PBAs (Fig. S6 in the ESI†) and the $Co_3Fe_4V_3O_x$ nanoparticles. Additionally, no N signal was detected in the metal oxide nanoparticles by EDX mapping and XPS (at about 400 eV), confirming the total thermal decomposition of the PBA nanoparticles. Table S3 in the ESI† shows that the elemental compositions determined by EDX, inductively-coupled plasma atomic emission spectroscopy (ICP-AES), and

XPS (Fig. S7†) are similar, indicating that the PBA nanoparticles are an efficient metal precursor to precisely control the elemental composition of the resulting metal oxide nanoparticles.

We further collected the Raman spectra of the trimetallic ($Co_3Fe_4V_3O_x$), bimetallic ($Co_5V_5O_x$ and $Co_6Fe_4O_x$) and unitary CoO_x (Fig. 2g) particles. Excluding the strong Raman peaks above 800 cm^{-1}, which are from V–O vibrations,[46] several distinctive Raman peaks of Co–O are observed. The A_{1g} mode at

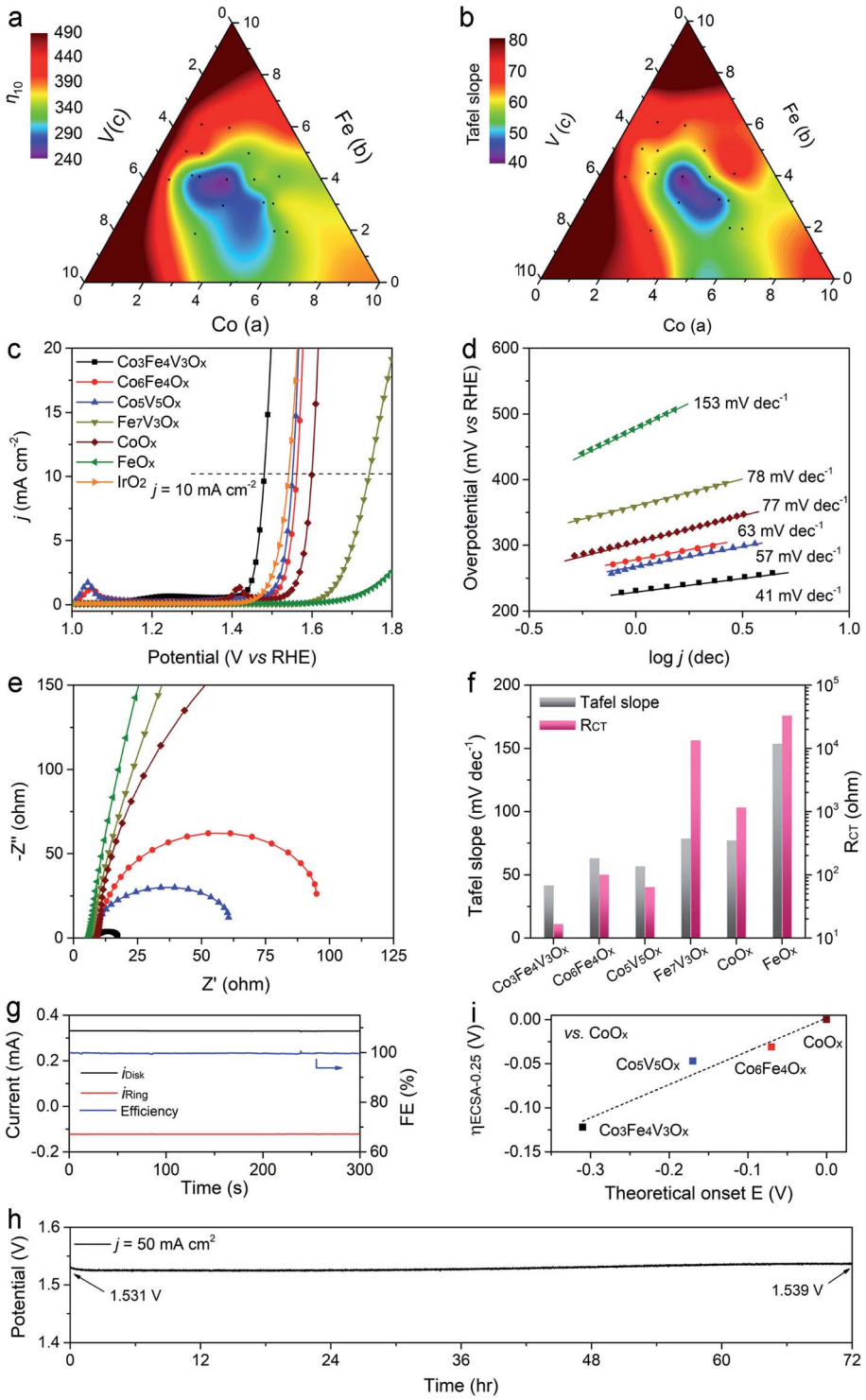

Fig. 3 OER performance atlas of ternary $Co_aFe_bV_cO_x$ in terms of (a) η_{10} and (b) Tafel slope based on the sample composition determined by ICP-AES and marked by black dots. (c) LSV curves, (d) Tafel plots, (e) EIS Nyquist plots, and (f) comparison of the Tafel slopes and R_{CT} of representative samples. (g) Faradaic efficiency and (h) stability test results of the optimal $Co_3Fe_4V_3O_x$. (i) The relationship between theoretical and experimental onset overpotentials of different samples *versus* the CoO_x catalyst and CoOOH model, respectively.

688 cm^{-1} can be assigned to octahedral sites while the E_g (462 cm^{-1}) and F_{2g} (517 and 610 cm^{-1}) peaks are from M–O vibrations in both octahedral and tetrahedral coordinations.[47] The much weaker E_g peak in $Co_3Fe_4V_3O_x$ indicates that Co atoms preferentially occupy octahedral sites ([CoO_6]). In comparison to the sharp and well-resolved Raman peaks in the unitary CoO_x, the prominent peak broadening and intensity reduction found in the bimetallic and trimetallic oxide samples indicate that the Co-coordination environment is defective and distorted. Based on these Raman results, we conclude that the incorporation of Fe and V leads to the formation of abundant defective [CoO_{6-a}] octahedral sites, which have been reported to be catalytically active sites for the OER.[48,49] In addition, the peak appearing at 292 cm^{-1} in the spectrum of $Co_6Fe_4O_x$ is indicative of the formation of an inverse spinel phase in which the ferrite cations occupy the tetrahedral sites.[47]

The OER activity of different $Co_aFe_bV_cO_x$ samples was evaluated in an O_2 saturated 1 M KOH alkaline electrolyte. All samples were loaded on glassy carbon electrodes (GCEs) with the same mass loading of 0.2 mg cm^{-2}. The well-defined structures of PBA nanoparticles enable us to synthesize ternary $Co_aFe_bV_cO_x$ with precisely controlled elemental compositions. Thus, we constructed OER catalytic performance atlases for ternary amorphous Co–Fe–V metal oxides. We used two criteria to compare their performance: (1) the overpotential required to reach a geometric current density (j) of 10 mA cm^{-2} (η_{10}, Fig. 3a) and (2) the Tafel slopes (Fig. 3b). All data points presented in Fig. 3a and b are listed in Table S4 in the ESI† and their LSV and Tafel plots are displayed in Fig. S8 in the ESI.† The optimal elemental composition required to achieve the highest OER catalytic activity is identified to have the molar ratio of Co : Fe : V at 3 : 4 : 3 from both atlases. This sample ($Co_3Fe_4V_3O_x$) exhibits the lowest η_{10} of 249 mV and the smallest Tafel slope of 41 mV dec^{-1}. Fig. 3c displays the LSV curves of $Co_3Fe_4V_3O_x$, bimetallic, and monometallic oxides (except VO_x) with the best performance, and IrO_2. The η_{10} of $Co_3Fe_4V_3O_x$ is 50 mV smaller than that of IrO_2 as well as RuO_2 (Fig. S9a in the ESI†). However, the crystal-phase segregated $Co_3Fe_4V_3O_x$-C sample showed a much reduced performance (Fig. S9b in the ESI†). The $Co_3Fe_4V_3O_x$ exhibited one of the best performances among recently reported Co– Fe–V-based OER catalysts. A detailed comparison is provided in Table S5 in the ESI.†

The Tafel slopes of the different samples are extracted from their Tafel plots in Fig. 3d. $Co_3Fe_4V_3O_x$ exhibits superior kinetic performance over other samples with the smallest slope of 41 mV dec^{-1}, suggesting a proton-electron coupled transfer step, for example, the formation of the O* intermediate, as the rate-limiting step.[50,51] Interestingly, the Tafel slope of $Co_5V_5O_x$ (57 mV dec^{-1}) is lower than that of $Co_6Fe_4O_x$ (67 mV dec^{-1}), suggesting that incorporating V is highly efficient in improving the kinetic performance of Co-based electrocatalysts. As shown in Fig. 3e, the charge transfer resistance (R_{CT}) of different samples at an η of 250 mV was determined from their electrochemical impedance (EIS) Nyquist plots by fitting with an equivalent circuit (Fig. S10 in the ESI†). The incorporation of Fe and/or V into Co oxides gradually reduces their R_{CT}. The optimal $Co_3Fe_4V_3O_x$ has the smallest R_{CT} of 16 Ohms (Table 1). Besides, $Co_5V_5O_x$ has a lower R_{CT} of 62 ohms than $Co_6Fe_4O_x$ at 97 Ohms, which agrees with their Tafel slopes as compared in Fig. 3f.

To accurately compare the intrinsic activity of our electrocatalysts, we further determined their electrochemically active surface area (ECSA) normalized current density (j_{ECSA}) to minimize the influence of different surface areas. The ECSA was determined by using the cyclic voltammetry method (Fig. S11 and S12 in the ESI†). A specific capacity of 0.04 mF cm^{-2} for metal oxide surfaces was used for the calculation.[28] Fig. S12 in the ESI† shows that the calculated ECSAs have small variations (less than 30%) among the different samples, confirming the excellent morphological control in our synthesis method. Fig. S13 in the ESI† shows the performance atlas based on j_{ECSA}, which exhibits a similar pattern to that in Fig. 3a, indicating that the superior OER performance of $Co_3Fe_4V_3O_x$ originates from its intrinsic activity rather than the large surface area. We also compared the intrinsic activity of different samples based on their TOF and mass activity. $Co_3Fe_4V_3O_x$ shows a TOF of 0.1146 s^{-1} and mass activity of 599.5 A g^{-1} at $\eta = 350$ mV, which is much higher than that of other $Co_aFe_bV_cO_x$ metal oxides as well as the IrO_2 and RuO_2 benchmarks (Table 1).

The faradaic efficiency of $Co_3Fe_4V_3O_x$ was measured by the rotating ring-disk electrode method (RRDE, see the Experimental section for details), and a near-unity efficiency was observed (Fig. 3g). $Co_3Fe_4V_3O_x$ also displays excellent stability in its OER activity (Fig. 3h). The overpotential required to maintain a current density of 50 mA cm^{-2} shows a negligible change over a 72 hour chronoamperometric test. After the OER stability test, TEM imaging (Fig. S14 in the ESI†) shows minor morphological changes, and $Co_3Fe_4V_3O_x$ retains its amorphous structure. However, elemental analysis by ICP-AES indicated that ~6.3 ±

Table 1 Summary of the catalytic performance of different metal oxides

Samples	η_{10}, mV	Tafel slope, mV dec^{-1}	R_{CT}, Ohms	Mass activity, A g^{-1}	TOF, s^{-1}
$Co_3Fe_4V_3O_x$	249 ± 6	41	16	599.5	0.1146
$Co_6Fe_4O_x$	345 ± 5	63	97	32.0	0.0061
$Co_5V_5O_x$	309 ± 8	57	62	36.6	0.0071
$Fe_7V_3O_x$	529 ± 14	78	13 030	1.5	0.0003
CoO_x	386 ± 11	77	1124	12.7	0.0025
FeO_x	>600	153	32 070	2.4	0.0004
IrO_2	314	62	—	161.2	0.0535
RuO_2	307	60	—	217.2	0.0706

2.3 at% of V was leached from $Co_3Fe_4V_3O_x$ after the stability test while the ratio between Co and Fe remained unchanged (Co : Fe : V = 2.98 : 4.09 : 2.90). The ECSA of $Co_3Fe_4V_3O_x$ increases by about 15% after the stability test (Fig. S15 in the ESI†). These results suggest that the leaching of V from $Co_3Fe_4V_3O_x$ causes some minor surface reconstruction. Finally, we compared the experimentally measured onset potentials of different samples to our DFT calculations (Table S6 in the ESI†). The onset overpotential is defined as the overpotential required to reach an ECSA normalized current density of 0.25 mA cm^{-2} ($\eta_{ECSA\text{-}0.25}$, see Fig. S16 in the ESI†). As shown in Fig. 3i, there is an excellent agreement of the shifting trends between the experimentally measured and theoretically predicted results, as compared to the CoO_x reference, which validates our initial computational predictions.

The performance atlases in Fig. 3a and b suggest that the elemental composition has a significant impact on the OER catalytic activity of $Co_aFe_bV_cO_x$. We hypothesize that strong electronic interactions among the different metal atoms can tune the electronic structure of Co to enable efficient adsorption and desorption of OER intermediates, which contributes to the observed superior catalytic activity of $Co_3Fe_4V_3O_x$. To validate this hypothesis, we used XPS to probe the electronic structures of Co, Fe, and V in different metal oxides. The population of different valence metal cations is determined by deconvolution of the XPS spectra and the results are listed in Table S7 in the ESI.†[52,53] As displayed in Fig. 4a, the Co 2p spectra of all samples exhibited spin-orbit split peaks of Co 2p2/3 at 780 eV and 2p1/2 at 795 eV, respectively. The deconvolution of the Co $2p_{3/2}$ peaks indicates the co-existence of Co^{2+} (781.9 eV) and Co^{3+} (779.9 eV) in all samples. Co^{2+} is the major species in both $Co_3Fe_4V_3O_x$ (73.9 at%) and $Co_5V_5O_x$ (89.6 at%), while Co^{3+} is dominant in $Co_6Fe_4O_x$ (51.4 at%) and CoO_x (58.7 at%), suggesting that the electronic structure of Co can be affected by Fe and V. The analysis of Fe $2p_{3/2}$ features (711 eV, Fig. 4b) shows that the Fe^{3+} (711.2 eV) population is higher in $Co_3Fe_4V_3O_x$ (81.3 at%) and $Fe_7V_3O_x$ (96.6 at%) than in $Co_6Fe_4O_x$ (75.8 at%) and FeO_x (74.2 at%). As shown in Fig. 4c, the V 2p3/2 peak (517 eV) can be deconvoluted into three constituent peaks, including V^{3+} (515.6 eV), V^{4+} (516.7 eV) and V^{5+} (517.8 eV).[52,54] A higher fraction of V^{3+} can be found in $Co_3Fe_4V_3O_x$ (13.2 at%) and $Fe_7V_3O_x$ (15.4 at%). The bimetallic $Fe_7V_3O_x$ contains the highest amount of V^{4+} (76.5 at%) in comparison to the 62.3 at% in $Co_3Fe_4V_3O_x$ and 69.4 at% in $Co_5V_5O_x$. Its V^{5+} abundance (8.0 at%) is much smaller than the 24.5 and 26.5 at% in $Co_3Fe_4V_3O_x$ and $Co_5V_5O_x$, respectively. In addition, the O 1s features in these samples revealed the co-existence of the M–O bond (530.0 eV) and vacant O (O_{vac}, 531.8 eV) as a result of their amorphous crystallinity (Fig. S17 in the ESI†).[55,56] The deconvolution result suggests that these metal oxides exhibit a comparable O_{vac} population (34.7% to 42.2%).

Based on our XPS analysis, we proposed electronic interactions among the three metal species, as illustrated in Fig. 4d. First, V ions can extract electrons from their neighboring Fe cations *via* the bridging O, which is evident from the higher

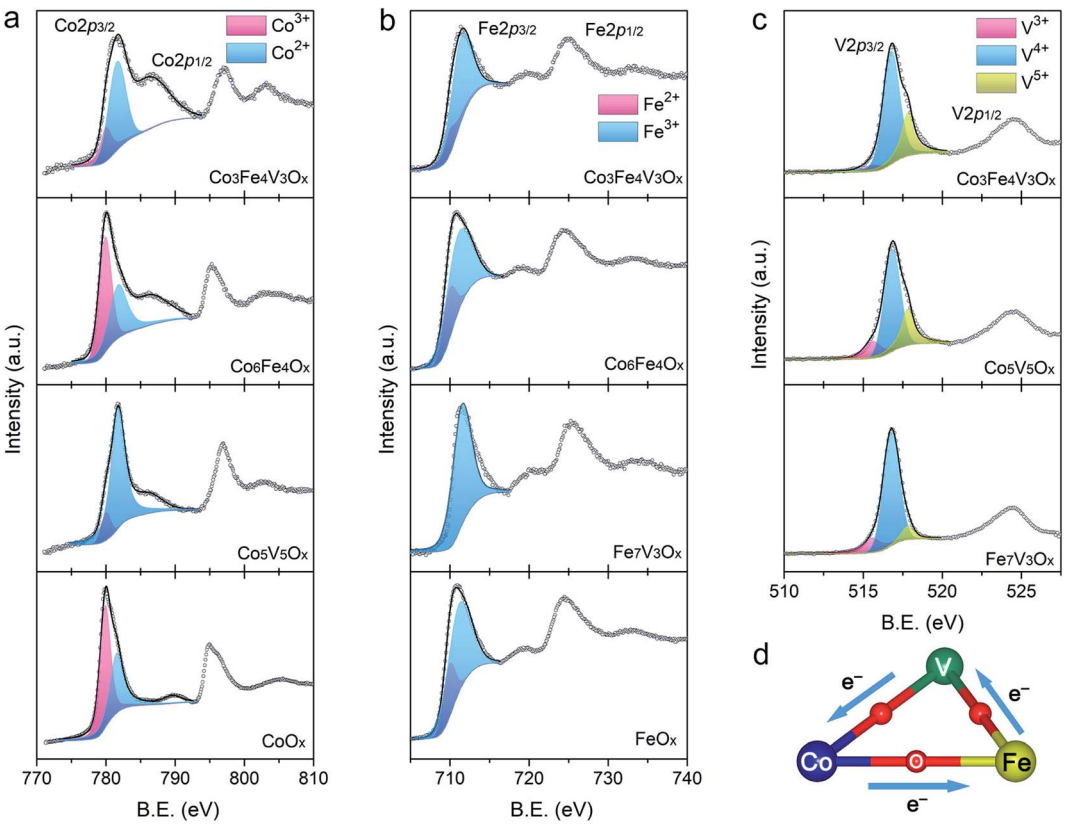

Fig. 4 High-resolution XPS spectra of (a) Co 2p, (b) Fe 2p and (c) V 2p for different $Co_aFe_bV_cO_x$. (d) A schematic illustration showing the proposed electronic interactions among Co, Fe, and V in $Co_aFe_bV_cO_x$.

fraction of Fe^{3+} in $Fe_7V_3O_x$ (96.6 at%) in comparison to the monometallic FeO_x (74.2 at%). Second, V may donate electrons to Co. This is supported by the highest average V valence state (4.22) in bimetallic $Co_5V_5O_x$ and the highest Co^{2+} abundance in $Co_5V_5O_x$ (89.6 at%) among all the samples. Last, Fe may withdraw electrons from Co as confirmed by the increased Co^{3+} abundance in the $Co_3Fe_4V_3O_x$ sample in comparison to the $Co_5V_5O_x$ sample, which also agrees with previous reports.[45,57]

To further verify the proposed electron transfer mechanism, we prepared two additional ternary $Co_aFe_bV_cO_x$ samples with a fixed Fe abundance ($b = 4$ or 40 at% Fe). The Co abundance was changed to 10 or 50 at%, denoted as $Co_1Fe_4V_5O_x$ and $Co_5Fe_4V_1O_x$, respectively. Their XPS spectra and analysis results are shown in Fig. S18 and listed in Table S7 in the ESI.† The analysis of their O 1s XPS features results in similar O_{vac} abundance (40.1 at% in $Co_1Fe_4V_5O_x$ and 38.5 at%% in $Co_5Fe_4V_1O_x$). We further plotted the calculated average valence states of Co, Fe, and V in ternary $Co_aFe_bV_cO_x$ against the abundance of Co in Fig. S19 in the ESI† to afford a qualitative comparison. While the abundance of Fe was held constant, the population of Co^{3+} and the changing trends in the average valence states of Co, Fe, and V agree well with our proposed electronic interaction mechanism. In $Co_1Fe_4V_5O_x$, the abundant V can donate electrons to Co, resulting in a slightly decreased average valence for Co at 2.22. V also withdraws electrons from Fe, which reduces the V valence to 3.95 and increases the Fe valence slightly to 2.86. When the Co abundance increases to 50 at%, Fe withdraws electrons from Co, effectively increasing the average valence of Co from 2.26 in $Co_3Fe_4V_3O_x$ to 2.52 in $Co_5Fe_4V_1O_x$, which is also close to the 2.51 of the $Co_5Fe_4O_x$ sample. Meanwhile, the abundant Co and Fe also affect the V, affording a higher V valence of 4.17. Our XPS analysis results suggest that the complex electronic interactions among Co, Fe, and V are highly sensitive to their composition. By systematically varying the composition of $Co_aFe_bV_cO_x$, we successfully identified the optimal $Co_3Fe_4V_3O_x$, which exhibits the highest OER activity because of its near-optimal electronic structures for the adsorption/desorption of reaction intermediates.

We also collected the high-resolution XPS spectra of Co, Fe, and V in $Co_3Fe_4V_3O_x$ after the OER stability test (Fig. S20 in the ESI†). While the Fe valence slightly increased (2.81 *vs.* 2.85), there was a significant increase in the abundance of Co^{3+} from 26.1 to 71.0 at% (Table S8 in the ESI†), suggesting that the majority of Co^{2+} transformed to OER active structures, for example, CoOOH.[32,33] V also exhibited significant changes with the formation of an abundance of high valence V species (20.1 at% of V^{4+} and 77.5 at% of V^{5+}). The formation of these higher valence V species is expected to facilitate electron extraction and benefit the OER.[58] The lineshape of the O 1s spectrum after the stability test also resembles that of the metal oxyhydroxide, confirming the formation of the OER active CoOOH phases at the metal oxide surface.[59]

Conclusion

In summary, our DFT calculations showed that tuning the Fe and V doping in Co oxyhydroxide can significantly influence its catalytic activity for the OER. Guided by these theoretical results, we designed and synthesized a series of amorphous $Co_aFe_bV_cO_x$ with precisely controlled elemental compositions using PBA nanoparticles as metal precursors. These PBA nanoparticles have tuneable elemental compositions, and they can be converted into amorphous metal oxides *via* thermal decomposition in air at 300 °C. A catalytic activity atlas of amorphous $Co_aFe_bV_cO_x$ for the OER in an alkaline electrolyte was established by systematically studying $Co_aFe_bV_cO_x$ with varied elemental compositions. The optimal elemental composition was found at Co : Fe : V = 3 : 4 : 3. The optimal $Co_3Fe_4V_3O_x$ delivers a current density of 10 mA cm^{-2} at an overpotential of 249 mV, which is superior to that of the bimetallic and monometallic counterparts as well as a commercial IrO_2 catalyst. Additionally, $Co_3Fe_4V_3O_x$ showed excellent durability with negligible potential increments over a 72 h stability test. Detailed XPS analysis revealed that Fe and V doping effectively modulates the electronic structures of the Co active site in $Co_aFe_bV_cO_x$. The electronic structure of Co in $Co_3Fe_4V_3O_x$ has nearly optimal adsorption energies for reaction intermediates in the OER, resulting in its superior activity. The catalytic activity atlas provides a useful guide for OER electrocatalyst development. Further, taking advantage of the compositional versatility and uniformity of PBA precursors, more multi-metallic oxides can be explored for renewable energy applications.

Conflicts of interest

There are no conflicts to declare.

Acknowledgements

We acknowledge the financial support from the Australian Research Council under the Future Fellowships scheme (FT160100107) and the Discovery Programme (DP180102210). The calculations performed at the University of Texas were supported by the Welch Foundation (F-1841) and the Texas Advanced Computing Center.

References

1 X. C. Chen, Z. X. Yu, L. Wei, Z. Zhou, S. L. Zhai, J. S. Chen, Y. Q. Wang, Q. W. Huang, H. E. Karahan, X. Z. Liao and Y. Chen, *J. Mater. Chem. A*, 2019, 7, 764–774.
2 Z. X. Pei, Y. Huang, Z. J. Tang, L. T. Ma, Z. X. Liu, Q. Xue, Z. F. Wang, H. F. Li, Y. Chen and C. Y. Zhi, *Energy Storage Mater.*, 2019, **20**, 234–242.
3 Y. Jiao, Y. Zheng, M. Jaroniec and S. Z. Qiao, *Chem. Soc. Rev.*, 2015, **44**, 2060–2086.
4 N. T. Suen, S. F. Hung, Q. Quan, N. Zhang, Y. J. Xu and H. M. Chen, *Chem. Soc. Rev.*, 2017, **46**, 337–365.
5 Y. Dou, L. Zhang, J. Xu, C. T. He, X. Xu, Z. Sun, T. Liao, B. Nagy, P. Liu and S. X. Dou, *ACS Nano*, 2018, **12**, 1878–1886.
6 D. U. Lee, M. G. Park, H. W. Park, M. H. Seo, X. Wang and Z. Chen, *ChemSusChem*, 2015, **8**, 3129–3138.

7 Y. Wang, Y. Zhang, Z. Liu, C. Xie, S. Feng, D. Liu, M. Shao and S. Wang, *Angew. Chem., Int. Ed.*, 2017, **56**, 5867–5871.
8 T. Li, Y. Lv, J. Su, Y. Wang, Q. Yang, Y. Zhang, J. Zhou, L. Xu, D. Sun and Y. Tang, *Adv. Sci.*, 2017, **4**, 1700226.
9 F. Kong, K. Chen, S. Song and D. Xue, *Inorg. Chem. Front.*, 2018, **5**, 1962–1966.
10 Y. Feng, X. Y. Yu and U. Paik, *Sci. Rep.*, 2016, **6**, 34004.
11 Y. Zhang, X. Xia, X. Cao, B. Zhang, N. H. Tiep, H. He, S. Chen, Y. Huang and H. J. Fan, *Adv. Energy Mater.*, 2017, **7**, 1700220.
12 S. Ci, S. Mao, Y. Hou, S. Cui, H. Kim, R. Ren, Z. Wen and J. Chen, *J. Mater. Chem. A*, 2015, **3**, 7986–7993.
13 J. Meng, X. Liu, J. Li, Q. Li, C. Zhao, L. Xu, X. Wang, F. Liu, W. Yang, X. Xu, Z. Liu, C. Niu and L. Mai, *Nano Lett.*, 2017, **17**, 7773–7781.
14 Q. Zhang, X. L. Li, B. X. Tao, X. H. Wang, Y. H. Deng, X. Y. Gu, L. J. Li, W. Xiao, N. B. Li and H. Q. Luo, *Appl. Catal., B*, 2019, **254**, 634–646.
15 S. Li, S. Sirisomboonchai, A. Yoshida, X. An, X. Hao, A. Abudula and G. Guan, *J. Mater. Chem. A*, 2018, **6**, 19221–19230.
16 H. Yuan, S. Wang, X. Gu, B. Tang, J. Li and X. Wang, *J. Mater. Chem. A*, 2019, **7**, 19554–19564.
17 B. Zhang, X. L. Zheng, O. Voznyy, R. Comin, M. Bajdich, M. Garcia-Melchor, L. L. Han, J. X. Xu, M. Liu, L. R. Zheng, F. P. G. de Arquer, C. T. Dinh, F. J. Fan, M. J. Yuan, E. Yassitepe, N. Chen, T. Regier, P. F. Liu, Y. H. Li, P. De Luna, A. Janmohamed, H. L. L. Xin, H. G. Yang, A. Vojvodic and E. H. Sargent, *Science*, 2016, **352**, 333–337.
18 B. Sarkar, B. K. Barman and K. K. Nanda, *ACS Appl. Energy Mater.*, 2018, **1**, 1116–1126.
19 C.-C. Lin and C. C. L. McCrory, *ACS Catal.*, 2017, **7**, 443–451.
20 T. Gao, Z. Jin, M. Liao, J. Xiao, H. Yuan and D. Xiao, *J. Mater. Chem. A*, 2015, **3**, 17763–17770.
21 K. Chakrapani, G. Bendt, H. Hajiyani, T. Lunkenbein, M. T. Greiner, L. Masliuk, S. Salamon, J. Landers, R. Schlögl, H. Wende, R. Pentcheva, S. Schulz and M. Behrens, *ACS Catal.*, 2018, **8**, 1259–1267.
22 P. E. Blochl, *Phys. Rev. B*, 1994, **50**, 17953–17979.
23 J. P. Perdew, K. Burke and M. Ernzerhof, *Phys. Rev. Lett.*, 1996, **77**, 3865–3868.
24 B. Hammer, L. B. Hansen and J. K. Norskov, *Phys. Rev. B*, 1999, **59**, 7413–7421.
25 W. Kohn and L. J. Sham, *Phys. Rev.*, 1965, **140**, A1133.
26 H. J. Monkhorst and J. D. Pack, *Phys. Rev. B*, 1976, **13**, 5188–5192.
27 M. Bajdich, M. Garcia-Mota, A. Vojvodic, J. K. Norskov and A. T. Bell, *J. Am. Chem. Soc.*, 2013, **135**, 13521–13530.
28 C. C. L. McCrory, S. Jung, J. C. Peters and T. F. Jaramillo, *J. Am. Chem. Soc.*, 2013, **135**, 16977–16987.
29 H. Liu, Y. Wang, X. Lu, Y. Hu, G. Zhu, R. Chen, L. Ma, H. Zhu, Z. Tie, J. Liu and Z. Jin, *Nano Energy*, 2017, **35**, 350–357.
30 Y. Qiu, L. Xin and W. Li, *Langmuir*, 2014, **30**, 7893–7901.
31 Y. Liang, Y. Li, H. Wang and H. Dai, *J. Am. Chem. Soc.*, 2013, **135**, 2013–2036.
32 A. Bergmann, T. E. Jones, E. Martinez Moreno, D. Teschner, P. Chernev, M. Gliech, T. Reier, H. Dau and P. Strasser, *Nat. Catal.*, 2018, **1**, 711–719.
33 T. Wu, S. Sun, J. Song, S. Xi, Y. Du, B. Chen, W. A. Sasangka, H. Liao, C. L. Gan, G. G. Scherer, L. Zeng, H. Wang, H. Li, A. Grimaud and Z. J. Xu, *Nat. Catal.*, 2019, **2**, 763–772.
34 B. Zhang, X. Zheng, O. Voznyy, R. Comin, M. Bajdich, M. García-Melchor, L. Han, J. Xu, M. Liu, L. Zheng, F. P. García de Arquer, C. T. Dinh, F. Fan, M. Yuan, E. Yassitepe, N. Chen, T. Regier, P. Liu, Y. Li, P. De Luna, A. Janmohamed, H. L. Xin, H. Yang, A. Vojvodic and E. H. Sargent, *Science*, 2016, **352**, 333–337.
35 M. Bajdich, M. García-Mota, A. Vojvodic, J. K. Nørskov and A. T. Bell, *J. Am. Chem. Soc.*, 2013, **135**, 13521–13530.
36 K. Xu, P. Chen, X. Li, Y. Tong, H. Ding, X. Wu, W. Chu, Z. Peng, C. Wu and Y. Xie, *J. Am. Chem. Soc.*, 2015, **137**, 4119–4125.
37 I. C. Man, H. Y. Su, F. Calle-Vallejo, H. A. Hansen, J. I. Martinez, N. G. Inoglu, J. Kitchin, T. F. Jaramillo, J. K. Norskov and J. Rossmeisl, *Chemcatchem*, 2011, **3**, 1159–1165.
38 Z.-F. Huang, J. Wang, Y. Peng, C.-Y. Jung, A. Fisher and X. Wang, *Adv. Energy Mater.*, 2017, **7**, 1700544.
39 M. S. Burke, M. G. Kast, L. Trotochaud, A. M. Smith and S. W. Boettcher, *J. Am. Chem. Soc.*, 2015, **137**, 3638–3648.
40 J. Chen, L. Wei, A. Mahmood, Z. Pei, Z. Zhou, X. Chen and Y. Chen, *Energy Storage Mater.*, 2020, **25**, 585–612.
41 X. Su, Y. Wang, J. Zhou, S. Gu, J. Li and S. Zhang, *J. Am. Chem. Soc.*, 2018, **140**, 11286–11292.
42 Y. Feng, X. Wang, P. Dong, J. Li, L. Feng, J. Huang, L. Cao, L. Feng, K. Kajiyoshi and C. Wang, *Sci. Rep.*, 2019, **9**, 15965.
43 W. Ahn, M. G. Park, D. U. Lee, M. H. Seo, G. Jiang, Z. P. Cano, F. M. Hassan and Z. Chen, *Adv. Funct. Mater.*, 2018, **28**, 1802129.
44 W. Zhang, H. Song, Y. Cheng, C. Liu, C. Wang, M. A. N. Khan, H. Zhang, J. Liu, C. Yu, L. Wang and J. Li, *Adv. Sci.*, 2019, **6**, 1801901.
45 L. Wei, H. E. Karahan, S. Zhai, H. Liu, X. Chen, Z. Zhou, Y. Lei, Z. Liu and Y. Chen, *Adv. Mater.*, 2017, **29**, 1701410.
46 R. L. Frost, S. J. Palmer, J. Čejka, J. Sejkora, J. Plášil, S. Bahfenne and E. C. Keeffe, *J. Raman Spectrosc.*, 2011, **42**, 1701–1710.
47 N. Bahlawane, P. H. T. Ngamou, V. Vannier, T. Kottke, J. Heberle and K. Kohse-Höinghaus, *Phys. Chem. Chem. Phys.*, 2009, **11**, 9224–9232.
48 Y. Xu, F. Zhang, T. Sheng, T. Ye, D. Yi, Y. Yang, S. Liu, X. Wang and J. Yao, *J. Mater. Chem. A*, 2019, **7**, 23191–23198.
49 J. Liu, Y. Ji, J. Nai, X. Niu, Y. Luo, L. Guo and S. Yang, *Energy Environ. Sci.*, 2018, **11**, 1736–1741.
50 R. Doyle and M. Lyons, in *Photoelectrochemical Solar Fuel Production*, ed. S. Gimenez and J. Bisquert, Springer, Switzerland, 2016, Ch. 2, pp. 41–104.
51 M. E. Lyons and M. P. Brandon, *Int. J. Electrochem. Sci.*, 2008, **3**, 1425–1462.
52 M. C. Biesinger, L. W. M. Lau, A. R. Gerson and R. S. C. Smart, *Appl. Surf. Sci.*, 2010, **257**, 887–898.
53 M. C. Biesinger, B. P. Payne, A. P. Grosvenor, L. W. M. Lau, A. R. Gerson and R. S. C. Smart, *Appl. Surf. Sci.*, 2011, **257**, 2717–2730.

54 K. Fan, Y. Ji, H. Zou, J. Zhang, B. Zhu, H. Chen, Q. Daniel, Y. Luo, J. Yu and L. Sun, *Angew. Chem., Int. Ed.*, 2017, **56**, 3289–3293.
55 Z. Xiao, Y. Wang, Y.-C. Huang, Z. Wei, C.-L. Dong, J. Ma, S. Shen, Y. Li and S. Wang, *Energy Environ. Sci.*, 2017, **10**, 2563–2569.
56 T. Zhang, M.-Y. Wu, D.-Y. Yan, J. Mao, H. Liu, W.-B. Hu, X.-W. Du, T. Ling and S.-Z. Qiao, *Nano Energy*, 2018, **43**, 103–109.
57 L. Zhuang, L. Ge, Y. Yang, M. Li, Y. Jia, X. Yao and Z. Zhu, *Adv. Mater.*, 2017, **29**, 1606793.
58 J. Jiang, F. Sun, S. Zhou, W. Hu, H. Zhang, J. Dong, Z. Jiang, J. Zhao, J. Li, W. Yan and M. Wang, *Nat. Commun.*, 2018, **9**, 2885.
59 Z. Chen, C. X. Kronawitter, Y.-W. Yeh, X. Yang, P. Zhao, N. Yao and B. E. Koel, *J. Mater. Chem. A*, 2017, **5**, 842–850.